Supplement

1. *Supplementary figure to main text*

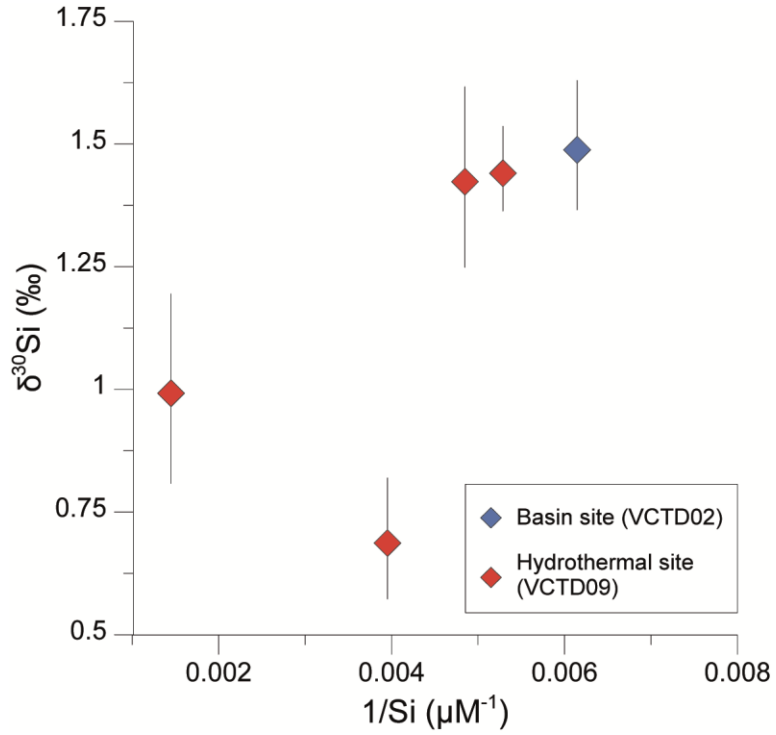

Fig. 1S: Hydrothermal plume $\delta^{30}Si$ versus the Si concentration. For comparison the $\delta^{30}Si$ of the basin site water column is shown. No correlation with the Si concentration can be observed.

2. *Supplementary tables to main text*

Table 1S: Pore fluid and sediment geochemistry data

		Pore fluid						Sediment		
Station/MUC#/ Station name	Latitude (N) / Longitude (W)	Depth	Cl	Mg	Na	K	NH_4	TC	TOC	$CaCO_3$
		(cmbsf)	(mM)	(mM)	(mM)	(mM)	(µM)	%	%	%
SO241-33/11/	27° 33.301'	0	*557.8*	*53.9*	10.0	473	*0.98*			
Basin site	111° 32.883'	0.5	*553.7*	*53.4*	10.3	470	*7.49*	4.3	3.9	3.6
		1.5	*555.9*	*53.2*	10.4	471	*13.58*	4.3	3.9	3.8
		2.5	*564.6*	*53.5*	10.6	472	*11.06*	4.3	3.7	5.1
		3.5	*562.6*	*53.6*	10.7	475	*12.06*	-	-	-
		4.5	*567.2*	*53.1*	10.6	472	*11.26*	4.2	3.6	4.5
		6	*569.9*	*53.1*	10.6	472	*13.05*	3.3	3.0	2.8
		8	*570.9*	*52.7*	10.7	470	*13.51*	-	-	-
		10	*569.9*	*52.4*	10.7	469	*12.92*	-	-	-
		12.5	*568.9*	*52.2*	10.9	468	*13.18*	3.8	3.1	5.7
		15.5	*573.5*	*51.9*	10.8	469	*17.02*	3.6	3.1	4.2
		18.5	*569.1*	*51.5*	10.7	466	*19.47*	-	-	-
		22	*573.2*	*51.4*	10.7	468	*18.15*	4.2	3.2	8.5
SO241-22/04/	27° 28.165'	0	*573.5*	*54.1*	10.0	478	*0.0*	-	-	-

Basin site	111° 28.347'	0.5	*554.1*	*53.6*	10.3	475	*4.9*	5.9	5.1	6.1
		1.5	*557.1*	*53.3*	10.3	474	*8.4*	-	-	-
		2.5	*559.7*	*53.2*	10.4	473	*11*	7.1	5.3	15
		3.5	*554.7*	*53.2*	10.3	473	*11*	-	-	-
		4.5	*556.4*	*53.2*	10.3	474	*25*	-	-	-
		5.5	*558.4*	*52.9*	10.3	471	*28*	5.9	5.3	5.1
		7	*556.9*	*53.3*	10.4	475	*35*	-	-	-
		9	*558.7*	*53.1*	10.4	473	*49*	5.8	5.2	4.6
		11	*561.3*	*53.1*	10.3	473	*36*	-	-	-
		13	*558.1*	*53.2*	10.3	473	*43*	-	-	-
		15.5	*558.7*	*53.3*	10.4	475	*44*	-	-	-
		18.5	*558.3*	*53.0*	10.4	473	*33*	6.1	5.7	3.9
		22	*556.6*	*53.0*	10.4	473	*28*	-	-	-
		26	*559.8*	*53.2*	10.4	475	*21*	3.9	3.5	3.8
SO241-23/05/	27° 30.282'	0	*560.4*	*55.3*	10.3	489	*0.3*	-	-	-
Basin site	111° 40.770'	0.5	*556.3*	*53.5*	10.1	474	*0.2*	5.0	3.4	13
		1.5	*552.2*	*53.7*	10.2	477	*5.6*	-	-	-
		2.5	*565.1*	*53.2*	10.3	474	*16*	-	-	-
		3.5	*557.3*	*53.5*	10.3	475	*19*	5.2	3.8	12
		4.5	*562.2*	*53.5*	10.4	476	-	-	-	-
		5.5	*557.4*	*53.3*	10.3	474	*28*	5.6	4.0	14
		7	*561.4*	*53.3*	10.3	473	*26*	-	-	-
		9	*563.2*	*53.7*	10.4	479	*29*	5.6	4.2	12
		11	*566.2*	*53.4*	10.4	476	*25*	-	-	-
		13	*563.3*	*53.3*	10.4	475	*27*	-	-	-
		15.5	*563.4*	*53.3*	10.4	474	-	7.1	3.4	31
		18.5	*561.5*	*53.4*	10.4	476	-	-	-	-
		22	*565.7*	*53.1*	10.4	473	*47*	7.8	3.3	38
SO241-15/02/	27°26.925'	0	*566.1*	*54.3*	10.1	479	*0.0*	-	-	-
Basin site	111°29.926'	0.5	*560.7*	*53.5*	10.2	474	*1.0*	3.5	2.9	4.5
		1.5	*559.8*	*53.6*	10.2	474	*0.0*	3.7	3.1	5.2
		2.5	*565.0*	*53.4*	10.3	473	*0.0*	4.1	3.4	5.1
		3.5	*561.9*	*53.6*	10.3	475	*0.0*	4.1	3.4	5.6
		4.5	*565.2*	*53.2*	10.3	473	*0.4*	3.9	3.2	5.4
		5.5	*564.5*	*53.3*	10.4	474	*1.3*	4.1	3.3	5.9
		7	*557.4*	*53.0*	10.4	472	*3.6*	4.0	3.3	6.1
		9	*557.6*	*53.1*	10.5	472	*6.7*	3.8	3.1	6.0
		11	*553.6*	*53.3*	10.4	472	*8.0*	3.5	2.8	5.8
		13	*560.1*	*53.3*	10.4	472	*10*	3.4	2.7	5.7
		15.5	*559.2*	*53.4*	10.3	473	*15*	2.5	2.0	4.6
		18.5	*559.5*	*53.4*	10.3	473	*22*	2.3	1.8	4.0
		22	*556.6*	*53.3*	10.4	474	*31*	3.7	3.1	5.5
		26	*556.8*	*53.2*	10.5	473	*42*	3.5	2.8	5.8
		30	*555.3*	*53.3*	10.9	477	*53*	3.0	2.6	3.9
SO241-66/16/	27° 24.577'	0	*546.4*	*54.4*	10.2	480	*0.0*	-	-	-
Hydrothermal	111° 23.265'	0.5	*556.7*	*53.5*	10.3	474	*5.0*	2.4	2.2	1.8
site		1.5	*550.6*	*53.7*	10.4	477	*10*	2.5	2.3	2.0
		2.5	*548.6*	*53.5*	10.4	474	*16*	2.4	2.0	2.9
		3.5	*548.4*	*53.5*	10.4	476	*17*	2.2	2.0	1.6
		4.5	*557.1*	*53.6*	10.4	477	*20*	2.2	1.8	3.1
		5.5	*547.2*	*53.5*	10.4	477	*20*	2.0	1.8	1.7
		6.5	*547.9*	*53.4*	10.4	475	*21*	1.9	1.7	1.6
		9	*546.8*	*53.8*	10.4	478	*22*	1.6	1.4	1.6

		11	*554.6*	*53.5*	10.3	474	*22*	1.1	1.0	0.4
		13	*548.2*	*53.5*	10.2	474	*22*	1.9	1.8	0.9
		15.5	*549.2*	*53.6*	10.2	475	*20*	2.2	2.1	1.3
		18.5	*554.7*	*53.7*	10.2	476	*20*	0.3	0.3	0.3
SO241-29/09/	27° 42.410	0	557.9	54.1	474	10.1	4.7	-	-	-
OMZ site	111° 13.656	0.5	553.1	53.7	471	10.2	24	3.5	2.8	5.7
		1.5	552.6	53.7	471	10.2	50	3.9	3.1	6.8
		2.5	558.8	53.4	468	10.1	68	4.1	3.3	7.0
		3.5	556.5	53.8	472	10.2	58	4.1	3.2	7.1
		4.5	553.0	53.5	469	10.2	93	4.3	3.4	7.7
		5.5	551.2	53.8	475	10.3	73	4.6	3.5	8.9
		6.5	553.3	53.3	467	10.2	92	4.4	3.5	7.3
		7.5	552.6	53.5	471	10.2	139	4.2	3.4	6.9
		9	554.0	53.6	471	10.3	183	4.1	3.3	6.2
		11	553.7	53.7	472	10.3	218	4.0	3.4	5.0
		13	555.7	53.3	469	10.2	281	4.0	3.5	4.3
		15	557.7	53.4	471	10.3	320	4.0	3.4	5.1
		18.5	556.2	53.5	472	10.3	402	3.6	3.3	2.5
		20.5	551.8	54.2	477	10.5	480	3.8	3.5	2.3
		23.5	546.9	53.0	466	10.2	582	3.6	3.1	4.6
		26.5	551.3	52.9	465	10.2	606	4.0	3.4	5.3
		29	555.5	53.3	469	10.2	660	3.9	3.5	3.4
		30	556.2	53.4	469	10.2	702	3.5	3.2	2.4
		38	562.7	53.2	469	10.2	767	3.4	3.3	0.7

Italic numbers published in Geilert et al., 2018

Table 2S: Main mineral phases identified by XRD analysis in wt-% for the basin sites and the hydrothermal site.

Station/MUC#/ Station name	Depth	Quartz	Plagioclase	K-feldspar	Calcite	Mg-rich Calcite	Aragonite	Dolomite	Ankerite
Error (rel%)	(cmbsf)	±1	±2-5	±2-5	±1	±2-3	±2-3	±1	±2-3
SO241-33/11/	0.5	8.9	8.5	10.0	0.0	0.0	0.0	0.0	0.0
Basin site	2.5	6.2	5.4	7.6	0.0	0.0	0.0	0.0	0.0
	12.5	8.3	9.9	0.0	0.0	0.0	0.0	0.0	0.0
	22.0	7.7	9.2	5.1	0.0	0.0	0.0	0.0	0.2
SO241-22/04/	0.5	10.7	14.5	1.1	0.0	0.0	0.0	0.0	0.7
Basin site	5.5	14.0	16.6	4.9	0.0	0.0	0.0	0.0	0.7
	9.0	8.9	7.6	10.3	0.0	0.3	0.0	0.0	0.4
	18.5	9.5	10.4	13.6	0.0	0.0	0.0	0.0	0.6
	26.0	9.0	10.0	9.8	0.0	0.0	0.0	0.0	0.3
SO241-23/05/	0.5	7.2	8.4	0.0	0.0	0.0	0.0	0.0	0.4
Basin site	3.5	6.9	5.7	17.7	0.0	0.0	0.0	0.0	0.5
	9.0	8.5	6.6	4.6	0.0	0.0	0.0	0.3	0.0
	22.0	9.0	10.1	4.3	0.2	0.4	0.0	0.3	0.4
SO241-15/02/	0.5	3.0	6.2	5.7	0.0	0.0	0.0	0.2	0.3
Basin site	5.5	9.1	9.0	1.7	0.0	0.7	0.0	0.0	0.4
	15.5	15.5	8.2	0.0	0.0	0.4	0.0	0.1	1.0
	30.0	8.2	9.6	2.7	0.0	0.0	0.0	0.0	0.5
SO241-66/16/	0.5	2.0	19.8	5.8	0.0	0.0	0.0	0.0	0.0
Hydrothermal	2.5	9.1	9.8	19.5	0.0	0.0	0.0	0.2	0.3

site	5.5	7.8	12.3	10.7	0.4	0.4	0.0	0.4	0.4
	13.0	0.8	4.8	9.5	0.0	0.0	2.6	0.4	0.4
	18.5	1.9	12.5	22.9	0.5	0.5	0.0	0.7	0.2

Table 2S continued

Station/MUC#/ Station name	Depth	Smectites	Montmorillo -nites	Cristoballite	Trydimite	SiO2 nearly amorphous	Mixed Layer Clays	Illites	Muscovite	Biotite	Glauconite	Kaolinite	Chlorite
Error (rel%)	(cm bsf)	±5-10	±5-10	±2	±2	±5-10	±5-10	±5-10	±5-10	±5-10	±5-10	±2-5	±2-5
SO241-33/11/	0.5	0.0	5.0	0.0	0.0	23.9	20.3	5.9	1.7	0.0	0.0	1.9	1.0
Basin site	2.5	0.0	20.8	0.0	2.4	20.4	3.5	7.1	2.2	1.7	0.0	4.5	1.0
	12.5	1.4	6.6	0.0	0.0	22.6	25.0	7.0	0.0	0.0	0.0	1.9	0.8
	22.0	1.5	7.7	0.0	0.0	28.1	14.0	4.8	0.0	0.0	0.0	3.4	0.7
SO241-22/04/	0.5	3.4	7.2	0.0	0.0	8.0	2.3	26.0	0.0	0.0	0.0	4.9	1.0
Basin site	5.5	1.9	1.8	0.0	0.0	4.5	13.2	17.1	0.0	0.0	0.0	5.3	1.0
	9.0	0.5	7.4	0.0	0.0	5.0	7.3	36.6	0.0	1.5	0.0	4.5	1.0
	18.5	0.0	6.6	0.7	0.0	4.4	0.0	20.9	0.0	6.0	0.0	4.1	3.0
	26.0	0.0	7.1	0.0	0.0	4.7	7.6	10.9	2.9	2.0	0.0	6.0	0.8
SO241-23/05/	0.5	1.3	2.4	2.7	0.0	35.8	9.6	6.7	0.0	0.0	3.3	3.5	0.6
Basin site	3.5	6.3	5.2	0.0	0.0	41.0	5.5	8.7	0.0	0.0	4.3	6.4	0.5
	9.0	1.7	4.6	0.0	0.0	25.4	11.8	9.8	0.0	0.0	1.8	4.7	1.1
	22.0	1.1	4.0	0.0	0.0	23.0	15.4	5.6	0.0	0.0	0.0	5.9	0.7
SO241-15/02/	0.5	1.2	6.3	0.0	0.0	10.2	25.9	0.0	0.0	0.0	0.0	1.7	2.8

Basin site	5.5	2.9	7.5	0.0	0.0	28.6	8.6	12.6	0.0	0.0	0.0	3.6	1.8
	15.5	0.0	0.0	0.0	0.0	57.1	0.0	4.8	4.2	0.0	0.0	3.0	1.0
	30.0	3.5	6.9	0.0	0.0	21.7	5.9	9.3	0.0	0.0	3.6	4.1	1.3
SO241-66/16/	0.5	0.0	5.7	0.0	0.0	42.8	0.0	12.8	0.0	0.0	0.0	3.0	0.7
Hydrothermal site	2.5	2.6	8.0	1.6	1.6	25.3	5.0	14.3	0.0	0.0	1.4	3.9	0.6
	5.5	0.0	12.3	0.0	0.0	26.2	19.9	0.0	0.0	0.0	0.0	5.4	0.3
	13.0	0.0	1.9	0.0	0.0	42.2	4.0	5.1	0.0	0.0	0.0	3.0	2.5
	18.5	0.0	4.4	0.0	0.5	40.4	5.0	4.4	0.0	0.0	0.0	2.3	0.6

Table 2S continued

Station/MUC#/ Station name	Depth	Clino-Pyroxenes	Ortho-Pyroxenes	Pyrites	Fe-Oxides Fe-Hydroxides, Manganit	Barite
Error (rel%)	(cm bsf)	±2-5	±2-5	±2-5	±5-10	±2-5
SO241-33/11/	0.5	1.05	8.25	0.00	0.40	0.00
Basin site	2.5	1.45	2.82	2.44	0.00	0.00
	12.5	0.00	5.21	0.00	0.00	0.00
	22.0	4.71	0.00	3.67	1.33	0.00
SO241-22/04/	0.5	4.99	0.00	0.00	2.55	0.00
Basin site	5.5	3.98	0.00	0.15	2.56	0.00
	9.0	0.00	0.00	0.00	3.57	0.00
	18.5	5.70	0.87	6.50	1.49	0.00
	26.0	3.74	0.84	0.00	0.86	0.00

SO241-23/05/ Basin site	0.5	0.00	0.00	0.19	9.49	0.18
	3.5	0.00	0.00	0.34	0.77	0.00
	9.0	2.03	0.00	0.00	4.17	0.00
	22.0	0.65	0.00	0.00	3.73	0.00
SO241-15/02/ Basin site	0.5	0.00	13.78	4.33	3.09	0.00
	5.5	3.13	0.00	0.00	0.51	0.00
	15.5	1.10	0.00	1.77	0.29	0.36
	30.0	0.57	0.00	0.25	0.43	0.00
SO241-66/16/ Hydrothermal site	0.5	0.00	0.00	0.48	1.74	1.21
	2.5	0.00	2.58	0.00	2.37	0.00
	5.5	0.00	0.00	0.00	1.03	0.19
	13.0	0.00	4.59	3.58	0.23	1.38
	18.5	1.07	1.82	0.53	0.00	1.79

3. Model set-up

The turnover of solids (S) and dissolved species (P) was simulated applying the following mass balance equations:

$$d_S \cdot (1-\Phi) \cdot \frac{\partial S}{\partial t} = \frac{\partial}{\partial x}\left(d_S \cdot (1-\Phi) \cdot \left(D_B \cdot \frac{\partial S}{\partial x} - w \cdot S \right)\right) + d_S \cdot (1-\Phi) \cdot R_S$$

$$\Phi \cdot \frac{\partial P}{\partial t} = \frac{\partial}{\partial x}\left(\Phi \cdot \left(D_S \cdot \frac{\partial P}{\partial x} - v \cdot P \right)\right) + \Phi \cdot R_D$$

with S: concentration of solid species in dry sediment (g g^{-1}), P: concentration of dissolved species in pore water (µmol cm^{-3}), t: time (yr), x: sediment depth (cm), d_S: density of dry solids (d_S = 2.5 g cm^{-3}), Φ: porosity, D_B: bioturbation coefficient (cm^2 yr^{-1}); w: burial velocity of solids (cm yr^{-1}); R_S: turnover rates of solid species (g g^{-1} yr^{-1}), R_D: turnover rates of dissolved species (mmol cm^{-3} yr^{-1}), D_S: molecular diffusion coefficient of dissolved species in sediment pore water (cm^2 yr^{-1}); v: burial velocity of pore water (cm yr^{-1}).

The model was set up for 5 solid species (SiO_2 in biogenic opal, SiO_2 in authigenic phases formed in the sediment, K in sediments, $^{30}SiO_2$ in biogenic opal, $^{30}SiO_2$ in authigenic phases) and 3 species dissolved in porewater (silica, ^{30}Si-silica, K).

At the upper boundary of the model (x = 0), constant fluxes (rain rates RR_S) were applied for the solids:

$$d_S \cdot (1-\Phi) \cdot \left(-D_B \cdot \frac{\partial S}{\partial x} + w \cdot S \right)\Big|_{x=0} = RR_S$$

whereas constant concentrations corresponding to ambient bottom water values (P_{BW}) were used for the solutes:

$$P|_{x=0} = P_{BW}$$

A zero gradient condition was applied at the lower boundary (x = L) for both solids and solutes:

$$\frac{\partial S}{\partial x}\Big|_{x=L} = 0 \qquad \frac{\partial P}{\partial x}\Big|_{x=L} = 0$$

The model was solved using the solver for partial differential equations of MATHEMATICA applying the Method-of-Lines approach. The model was integrated over time until a steady state was attained. The parameter values, depth-dependent functions, kinetic rate laws, and rate terms applied in the model are listed in tables S3- S6.

Within this modeling framework, we applied and extended a previously developed isotope model to simulate the reactive transport of dissolved silica in surface sediments (Ehlert et al., 2016). In this model, two separate mass balance equations (see above) were set up to simulate the turnover of total dissolved $^{30}SiO_2$ and SiO_2. The isotopic composition of the pore fluid was calculated as ratio of these two compounds (MF_{30} = $^{30}Si/Si$). Considering the abundance of the three Si isotopes ^{28}Si, ^{29}Si and ^{30}Si, the mol fraction MF_{30} is related to the commonly used isotope ratio (R_{30} = $^{30}Si/^{28}Si$) as:

$$R_{30} = \frac{MF_{30} \cdot R_{St30} \cdot (R_{St29} \cdot (c_R - 1) - 1)}{c_R \cdot MF_{30} \cdot R_{St29} + R_{St30} \cdot (MF_{30} - 1)}$$

with R_{St30} = 0.0341465, R_{St29} = 0.0507446 and c_R = 0.51 (Ehlert et al., 2016).

The $\delta^{30}Si$ value of the pore fluid (in ‰) is calculated from the ratio as:

$$\delta^{30}Si = \left(\frac{R_{30}}{R_{St30} - 1}\right) \cdot 1000$$

Opal data and the concentration and isotopic composition of dissolved silica determined in pore fluids were employed to constrain rates of opal and terrigenous phase dissolution and the precipitation rate of authigenic phases. The shift to negative values observed in the pore fluids ($\delta^{30}Si_{pf}$) within the top cm of the sediment column is caused by the dissolution of terrigenous phases depleted in ^{30}Si. We applied a $\delta^{30}Si_{terr}$ value of -2‰ to simulate the release of terrigenous clay Si into the pore fluids (Frings et al., 2016) and induce the negative shift observed in the data. Authigenic phases precipitating in marine sediments are depleted in ^{30}Si with respect to the pore fluids. We applied a fractionation factor of $\Delta^{30}Si_{Au}$ =-2‰ ($\Delta^{30}Si_{Au} = \delta^{30}Si_{au} - \delta^{30}Si_{pf}$) to simulate the impact of authigenic phase precipitation on

pore fluid composition as previously observed in Peruvian OMZ sediments (Ehlert et al., 2016). With this approach, the positive shift of $\delta^{30}Si_{pf}$ values observed below 1 cm sediment depth was reproduced in the model by a combination of opal dissolution and authigenic phase precipitation.

The kinetics of terrigenous phase dissolution is largely known (Wallmann et al., 2008). Since our data imply that most of the dissolution takes place within the top cm of the sediment, we apply a dissolution rate that decreases exponentially with sediment depth (Fig. S2). Authigenic mineral precipitation is probably linked to terrigenous phase dissolution because dissolved Al released from terrigenous phases supports the formation of authigenic Si-Al phases in marine sediments (Loucaides et al., 2010). Hence, the precipitation rate usually decreases with sediment depth (Loucaides et al., 2010). Since the reactivity of biogenic opal also decreases with sediment depth (Van Cappellen and Qiu, 1997), we assumed that the kinetic rate constants for authigenic phase precipitation and biogenic opal dissolution decrease exponentially with depth and applied a solubility control to simulate the rates (Fig. S2, Tab. S5).

K/Al ratios measured in the solid phase and pore water K data were used as additional model constraints. We did not separate the pore water from the sediment prior to the solid phase K analysis. Hence, the K concentrations measured in the dried sediment samples were corrected for the contribution of K dissolved in pore fluids applying the following equation:

$$K_C = K_M - \frac{f_W}{1 - f_W} K_{PW}$$

where K_C is the concentration of K in the solid phase (g/g) corrected for the pore water contribution, K_M is the concentration of K measured in dried samples (g/g), f_W is the initial water content of the wet samples prior to drying (g/g) and K_{PW} is the concentration of dissolved K in the pore water (g/g). The concentration of K in pore water was measured in units of mmol/dm^3. It was converted into appropriate units (g/g) by multiplying with the factor 10^{-6} MW_K where MW_K is the molecular weight of K.

The release of K during the dissolution of terrigenous clay phases and the uptake of K in authigenic phases was simulated applying corresponding K/Si ratios. Unfortunately, we did not determine the Si content of the OMZ sediments. Moreover, the total Si content in OMZ sediments reflects not only the terrigenous contribution but also the concentrations of biogenic opal and authigenic phases. The mean K/Al ratio measured in our OMZ sediments (0.33 g/g, after correction for pore water K) is close to the K/Al ratio in shale (0.34 g/g) and upper continental crust (0.35 g/g) (Wedepohl, 1971; Taylor and McLennan, 1995). Hence, we applied the mean K/Si ratio of shale and upper continental crust to simulate the K release from terrigenous phases (K/Si_{Terr} = 0.1 g/g = 0.07 mol/mol). Authigenic Si phases formed in marine sediments are typically enriched in K and we applied the K/Si of authigenic material in Amazon sediments (Michalopoulos and Aller, 2004) to define the uptake of K in authigenic phases (K/Si_{Au} = 0.19 mol/mol).

Moreover, we applied a constant Al concentration in the model corresponding to the mean Al concentration measured in the OMZ sediments (4.8 ± 0.5 wt-%). We assumed a constant Al deposition rate at the sediment surface and that Al released from sediments during mineral dissolution was quantitatively re-precipitated in authigenic minerals. The solid phase K concentrations calculated in the model were normalized to the mean Al concentration measured in the sediment and compared to the measured K/Al ratios. With this approach, we assume that any down-core change in the Al concentration observed in the data is induced by processes that are not considered in the model such as temporal changes in the composition and mass accumulation rate of terrigenous phases deposited at the sediment surface.

A best fit model solution was obtained by fitting the model results to dissolved silica concentrations and $\delta^{30}Si$ values measured in the pore fluids and the biogenic opal and K/Al ratios measured in the solid phase corrected for pore water K. Down-core changes in kinetic rate constants (Fig. S2), rain rates of biogenic opal and solid phase K at the sediment surface and the solubility of the authigenic phase were varied systematically to obtain the best fit to the observations. However, our model results should be regarded with caution because we applied strongly simplifying assumptions (e.g. steady state, simple rate laws). Moreover, our estimates of solid phase reactivity and isotopic composition are preliminary and not supported by independent data.

Tab. S3. Parameter values applied in the model

Parameter	**Symbol**	**Value**
Density of dry solids	d_S	2.5 g cm^{-3}
Porosity at x = 0	Φ_0	0.97
Porosity at x = infinity	Φ_f	0.91
Attenuation coefficient for porosity decrease	px	0.15 cm^{-1}
Bioturbation coefficient at x = 0	$D_B(0)$	1 cm^2 yr^{-1}
Depth of bioturbated zone	x_B	1 cm
Burial velocity after compaction	w_f	0.18 cm yr^{-1}
Sediment temperature	T	6.7 °C
Salinity of porewater	Sal	35
Molecular diffusion coefficient for dissolved silica	D_M	188 cm^2 yr^{-1}
Molecular diffusion coefficient for dissolved K	D_M	388 cm^2 yr^{-1}
Solubility of biogenic opal	Sol_{opal}	0.8 mM
Solubility of authigenic phase	Sol_{au}	0.2 mM
Rain rate of biogenic opal	RR_{opal}	7.3 mg cm^{-2} yr^{-1}
Rain rate of K	RR_K	0.77 mg cm^{-2} yr^{-1}
Molar K/Si ratio in terrigenous phase	K/Si_{terr}	0.07
Molar K/Si ratio in authigenic phase	K/Si_{au}	0.19
δ^{30}Si of opal deposited at the seafloor	$\delta^{30}Si_{opal}$	+0.77 ‰
δ^{30}Si of terrigenous phase subject to dissolution	$\delta^{30}Si_{terr}$	-2.0 ‰
Isotopic fractionation factor for authigenic phase formation	$\Delta^{30}Si_{au}$	-2.0 ‰
Isotopic fractionation factor for authigenic phase formation in term of mol fractions	β_{au}	0.998111
Molecular weight of SiO_2	MW_{SiO2}	60.08 g mol^{-1}
Atomic weight of K	MW_K	39.098 g mol^{-1}

Tab. S4. Depth-dependent functions applied in the model

Parameter	**Symbol**	**Equation**
Porosity	Φ	$\Phi = \Phi_f + (\Phi_0 - \Phi_f) \cdot \exp(-px \cdot x)$
Bioturbation coefficient	D_B	$D_B = D_B(0) \cdot \exp\left(-\frac{x^2}{2 \cdot x_B{}^2}\right)$
Burial velocity of solids	w	$w = w_f \cdot \frac{1-\Phi_f}{1-\Phi}$
Burial velocity of solutes	v	$v = w_f \cdot \frac{\Phi_f}{\Phi}$
Tortuosity	To	$To^2 = 1 - 2 \cdot ln(\Phi)$
Diffusion coefficient of solutes in porewater	D_S	$D_S = \frac{D_M}{To^2} + D_B$
Function to convert rates from g g^{-1} yr^{-1} to µmol cm^{-3} yr^{-1}	f_{sp}	$f_{sp} = d_S \cdot 10^6 \cdot \frac{1-\Phi}{\Phi \cdot MW}$
Mol fraction of Si	MF	$MF = \frac{^{30}Si}{Si}$

Table S5: Kinetic rate laws applied in the model

Reaction	**Symbol**	**Equation**
Biogenic opal dissolution in g g^{-1} yr^{-1}	R_{opal}	$R_{opal} = k_{opal} \cdot S_{opal} \cdot \left(1 - \frac{Si(OH)_4}{Sol_{opal}}\right)$
Dissolution of terrigenous phase in µmol cm^{-3} yr^{-1}	R_{terr}	$R_{terr} = k_{terr}$
Authigenic mineral precipitation in µmol cm^{-3} yr^{-1}	R_{au}	$R_{au} = k_{au} \cdot \left(\frac{Si(OH)_4}{Sol_{au}} - 1\right)$
Dissolution of $^{30}SiO_2$ in biogenic opal in g g^{-1} yr^{-1}	R_{opal}^{30}	$R_{opal}^{30} = MF_{opal} \cdot R_{opal}$
Dissolution of terrigenous $^{30}SiO_2$ in µmol cm^{-3} yr^{-1}	R_{terr}^{30}	$R_{terr}^{30} = MF_{terr} \cdot R_{terr}$
Precipitation auf authigenic $^{30}SiO_2$ in µmol cm^{-3} yr^{-1}	R_{au}^{30}	$R_{au}^{30} = MF_{pf} \cdot \beta_{au} \cdot R_{au}$

Table S6: Rate terms applied in mass balance equations

Species	**Equation**
Biogenic opal (in g g^{-1} yr^{-1})	$- R_{opal}$
Authigenic phase (in g g^{-1} yr^{-1})	$+ R_{au}/f_{sp}$
K in sediment (in g g^{-1} yr^{-1})	$(-K/Si_{terr} R_{terr} + K/Si_{au} R_{au})/f_{sp}$
Dissolved silica (in µmol cm^{-3} yr^{-1})	$f_{sp} R_{opal} + R_{terr} - R_{au}$
Dissolved K (in µmol cm^{-3} yr^{-1})	$K/Si_{terr} R_{terr} - K/Si_{au} R_{au}$
^{30}Si in authigenic phase (in g g^{-1} yr^{-1})	$+ R_{au}^{30}/f_{sp}$
^{30}Si in dissolved silica (in µmol cm^{-3} yr^{-1})	$f_{sp} R_{opal}^{30} + R_{terr}^{30} - R_{au}^{30}$

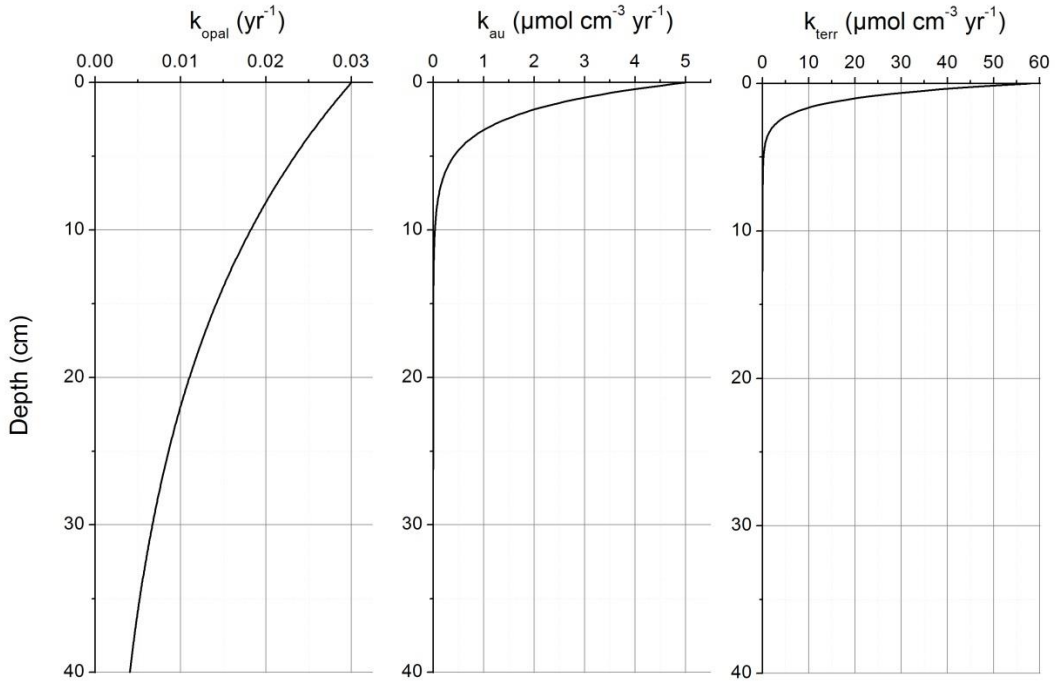

Fig. S2. Down-core profile of kinetic constants for biogenic opal dissolution (k_{opal}), authigenic phase precipitation (k_{au}) and terrigenous phase dissolution (k_{terr}) applied in the model runs

Supplementary references

Ehlert, C., Doering, K., Wallmann, K., Scholz, F., Sommer, S., Grasse, P., Geilert, S., and Frank, M.: Stable silicon isotope signatures of marine pore waters - Biogenic opal dissolution versus authigenic clay mineral formation, Geochimica Et Cosmochimica Acta, 191, 102-117, 10.1016/j.gca.2016.07.022, 2016.

Frings, P. J., Clymans, W., Fontorbe, G., De La Rocha, C. L., and Conley, D. J.: The continental Si cycle and its impact on the ocean Si isotope budget, Chemical Geology, 425, 12-36, 10.1016/j.chemgeo.2016.01.020, 2016.

Loucaides, S., Michalopoulos, P., Presti, M., Koning, E., Behrends, T., and Cappellen, P. V.: Seawater-mediated interactions between diatomaceous silica and terrigenous sediments: Results from long-term incubation experiments, Chemical Geology, 270, 68-79, 2010.

Michalopoulos, P., and Aller, R. C.: Early diagenesis of biogenic silcia in the Amazon delta: Alteration, authigenic clay formation, and storage, Geochimica et Cosmochimica Acta, 68, 1061-1085, 2004.

Taylor, S. R., and McLennan, S. M.: The geochemical evolution of the continental crust, Reviews of Geophysics, 33, 241-265, 1995.

Van Cappellen, P., and Qiu, L.: Biogenic silica dissolution in sediments of the Southern Ocean. II. Kinetics, Deep-Sea Research II, 44, 1129-1149, 1997.

Wallmann, K., Aloisi, G., Haeckel, M., Tishchenko, P., Pavlova, G., Greinert, J., Kutterolf, S., and Eisenhauer, A.: Silicate weathering in anoxic marine sediments, Geochimica et Cosmochimica Acta, 72, 2895-2918, 10.1016/j.gca.2008.03.026, 2008.

Wedepohl, K. H.: Environmantal influences on the chemical composition of shales and clay, Physics and Chemistry of the Earth, 8, 307-333, 1971.